Completely Automated Multi-resolution Edge Snapper (CAMES) – A New Technique for an Accurate Carotid Ultrasound IMT Measurement: Clinical Validation and Benchmarking on a Multi-Institutional Database

Filippo Molinari[1] *PhD,* Constantinos Pattichis[2]*, PhD*, Guang Zeng[3], *PhD*,

Luca Saba[4], *MD*, U Rajendra Acharya[5], *PhD.*, Roberto Sanfilippo[6], *MD*,

Andrew Nicolaides[7], *MS, FRCS, PhD (Hon)* and Jasjit S. Suri[8,9] *PhD, Fellow AIMBE*

[1] Biolab, Department of Electronics, Politecnico di Torino, Torino, Italy.

[2] Department of Computer Science, University of Cyprus, Nicosia, Cyprus.

[3] Mayo Clinic, Rochester, MN, USA.

[4] Department of Radiology, Azienda Ospedaliero Universitaria (A.O.U.), di Cagliari, Italy

[5] Department of ECE, Ngee Ann Polytechnic, Singapore

[6] Department of Surgery - UO Vascular and Thoracic Surgery (A.O.U.), di Cagliari, Italy

[7] CTO, Global Biomedical Technologies Inc., Roseville, CA, USA and Idaho State University (Aff), Pocatello, ID, USA.

CORRESPONDING AUTHOR: Professor Filippo Molinari, PhD
Biolab – Dipartimento di Elettronica, Politecnico di Torino
Corso Duca degli Abruzzi, 24, 10129 Torino, Italy
Phone: +39 11 090 4135 ; Fax: +39 11 090 4217 ; Email: filippo.molinari@polito.it

Abstract

The aim of this paper is the description of a novel and completely automated technique for carotid artery recognition, far (distal) wall segmentation, and intima-media thickness (IMT) measurement, a strong clinical tool for risk assessment for cardiovascular diseases.

The architecture of Completely Automated Multi-resolution Edge Snapper (CAMES, a patented class of AtheroEdge™ systems) consists of two stages: (a) automated carotid artery recognition based on a combination of scale-space and statistical classification in multi-resolution framework; and (b) automated segmentation of lumen-intima (LI) and media-adventitia (MA) interfaces for the far (distal) wall and (c) its IMT measurement.

Our database of 365 B-Mode longitudinal carotid images is taken from four different institutions covering different ethnic backgrounds. The ground-truth database was the average manual segmentation from three clinical experts. The mean distance ± SD of CAMES w.r.t ground-truth profiles for the LI and MA interfaces were 0.081 ± 0.099 mm and 0.082 ± 0.197 mm respectively. The IMT measurement error between CAMES and ground truth was 0.078 ± 0.112 mm. CAMES was benchmarked against a previously developed automated technique based on an integrated approach using feature-based extraction and classifier (CALEX). Even though, CAMES underestimated the IMT value, it had shown a strong improvement in segmentation errors against CALEX for LI and MA interfaces by 8% and 42%, respectively. The overall IMT measurement bias for CAMES improved against CALEX by 36%. Finally, the paper demonstrated that the figure-of-merit of CAMES was 95.8% compared to 87.4% for CALEX.

The combination of multi-resolution carotid artery recognition and far wall segmentation led to an automated, low-complexity, real-time, and accurate technique for carotid IMT measurement. Validation on a multi-ethnic/multi-institutional dataset demonstrated the robustness of the technique, which can constitute a clinically valid IMT measurement for assistance in atherosclerosis disease management.

Keywords: ultrasound imaging, carotid artery, multi-resolution, higher order derivative, lumen, intima-media thickness, automation.

I. Introduction

The intima-media thickness (IMT) of the carotid artery (CA) is a widely accepted and validated marker of progression of atherosclerosis and of onset of cardiovascular disorders, with a predictive value for incident myocardial infarction [1].

IMT is usually measured by using ultrasound imaging. Normally, a trained sonographer manually measures the IMT from longitudinal projections of the CA, but these manual measurements methods are time-consuming, subjective, and tedious. Also, due to the lack of standardization, the differences in the gain settings, scanner performances, and the training of the clinicians, all add up to cause significant variability, especially in large and multi-center studies. Figure 1 shows an example of B-Mode longitudinal carotid ultrasound image, with the far wall IMT measurement depicted.

Since early nineties, more than 30 different computer techniques were developed for the segmentation of the CA wall in longitudinal images (a state-of-the-art review on the most used image processing techniques in carotid wall segmentation and IMT measurement can be found in a recent review by Molinari *et al.* [2]). Conceptually, there are two main groups of computer methods for IMT measurement: group one comprises of all the techniques that are completely or fully automated, while group two are those that require user interaction or semi-automated. Usually, user-dependent methods offer better performance in IMT measurement, allowing measurement errors lower than 0.01 mm (an error in the range 1.25 - 2.5%, since the normal value of IMT is about 0.4 mm at birth and 0.8 mm at 80 years if no vascular pathologies are present [3]). The most popular image processing techniques for CA wall segmentation and IMT measurement are based on image gradients and edge-detection [4-6] or parametric deformable models (so called snakes) [7-9]. These detection techniques are faster than others, but suffer in general from noise. Also, they require user interaction for the region-of-interest (ROI) delineation around the distal (far) carotid wall.

The aim of this paper is the development of a high-performance automated technique for carotid IMT measurement. We present a new strategy based on a two cascaded stage process. Stage-I: that combines an edge detection approach based on scale-space paradigm in a multi-resolution framework; and Stage-II: segmentation of lumen-interface (LI) and media-adventitia (MA) borders for the far wall using a combination of first order absolute moment filtering followed by edge detection using Heuristics-based strategy.

Stage-I comprises of edge estimation for the far adventitia borders along the carotid artery. This edge estimation uses derivatives of Gaussian Kernels with known scales. The image processing paradigm comprises of optimization of the right Kernel size by reverse engineering the image framework itself. This can be accomplished in a multi-resolution framework. Stage-II comprises of an edge detector based on the first absolute central moment (originally adapted by Faita *et al.* [4]) adapted in the guidance zone or region of interest followed by Heuristics-based peak detection and location.

We named our new technique as CAMES: ***C****ompletely* ***A****utomated* ***M****ulti-resolution* ***E****dge* ***S****napper*, as we used edge information in multi-resolution framework for both recognition and segmentation phases. Special precaution based on anatomic arterial information, extracted using statistical intensity distribution is embedded in Stage-I to ensure 100% accuracy during the automated recognition phase. We validated CAMES on a multi-ethnic, multi-institutional database of 365 images, comprising of normal and pathologic CAs. Finally, we benchmarked CAMES against CALEX, our previously developed automated technique [10, 11]. Note, that the paper is not focused on segmentation of plaque borders having stenosis in carotid artery, rather the segmentation of far (distal) LI and far (distal) MA borders for automated, accurate and repeatable IMT measurements. Segmentation of plaque stenosis borders will be presented elsewhere.

II. Materials and Methods

A. Image dataset

Our database consisted of 365 B-mode images collected from four different institutions/hospitals around the world. They are: (i) The Neurology Division of the Gradenigo Hospital of Torino (Italy), which provided 200 images; (ii) The Cyprus Institute of Neurology of Nicosia (Cyprus), which provided 100 images; (iii) The Hospital de S. João do Porto (Portugal), which provided 23 images; (iv) The Department of Radiology of the University Hospital of Cagliari (Italy), which provided 42 images.

The complete description of the image database and of the patient's demographics is reported by Table I. All the images were acquired in digital format and discretized on 8 bits (256 gray levels). The conversion factors (*i.e.*, the physical pixel dimension which we indicate by τ in the paper and in Table I) ranged from 0.06 mm/pixel to 0.09 mm/pixel. The conversion factors were slightly different since they depended on the scanner type and scanner settings. Specifically, the images from Torino (200 images) and Nicosia (100 images) were resampled in order to set the pixel density to 16 pixels/mm and 16.67 pixels/mm, respectively, as already reported by previous studies [12, 13]. The two other Institutions allowed the sonographer to set the optimal pixel density and no resampling were performed.

The Institutions took care of obtaining written informed consent from the patients prior to acquiring data. The experimental protocol and data acquisition procedure were approved by the respective local Ethical Committees.

For each of the 365 images we had three manual segmentations made by expert sonographers (considered as ground truth – GT). To compute the IMT measurement bias, we obtained the average LI/MA tracings for every image.

*B. Architecture of the Multi-resolution Edge Snapper (*CAMES*)*

The architecture of CAMES was developed by keeping in mind that it should be able to locate the carotid artery in the image frame automatically and then segment the far wall of the carotid artery by computing the two interface boundaries: lumen-intima (LI) interface and media-adventitia (MA) interface. This recognition process must ensure that we are able to distinguish the carotid artery layer from other arteries or veins, in particular, the jugular vein (JV). We modeled the carotid artery recognition process by taking the hypothesis that carotid artery's far wall adventitia is the brightest in the ultrasound scan frame.

Our architecture for Stage-I is the recognition of the far adventitia location in the grayscale image of the carotid artery using multi-resolution approach in scale-space framework. Once the far adventitia layer of carotid artery is recognized, Stage-II can be adapted for LI and MA border estimation in the grayscale guidance zone near the far adventitia layer. In summary, our architecture consists of two cascaded stages in scale-space paradigm using multi-resolution framework adapting edge model approaches fused with Heuristics: (i) Automated recognition of the CA in the image frame, and (ii) Automated segmentation of the far (distal) CA wall, *i.e.,* LI and MA border estimation process.

Prior to recognition and segmentation phases, it is necessary to remove the non-relevant information in the image such as the patient and device. We developed a simple automated cropping procedure that automatically cropped the image in order to discard the surrounding black frame containing device headers and image/patient text data [14].

The 200 images from Torino were DICOM formatted, whereas all the other images were in TIFF or JPEG format and were auto-cropped by relying on the gradient strategy [14].

B.1 *Stage-I: Automatic Recognition of the Carotid Artery (CA)*

For the automated identification of the CA in the image frame we need to find the edges of the far adventitia borders using scale-space concept in multi-resolution framework. We need a fine to coarse down sampling followed by capturing the edges using derivative of Gaussian Kernel with known *a priori* scale. All the intermediate results of the processing steps are shown for the reference image shown in fig. 2.A.

Step 1: Fine to Coarse Down-sampling

The image was first down-sampled by a factor of two (*i.e.*, the number of rows and columns of the image was halved) (fig. 2.B). We implemented the down-sampling method discussed by Zhen *et al.* [15], adopting a bi-cubic interpolation that was tested on ultrasound images and showed a good accuracy and a low computational cost. The interpolated value is computed by considering the 16 pixels close to the considered one. Given a point *(x,y)* in the destination image *J(x,y)*, bi-cubic interpolation can be expressed as:

$$J(x,y) = \sum_{m=l-1}^{l+2} \sum_{n=k-1}^{k+2} I(m,n) \cdot r(m-l-dx) \cdot (dy-n+k) \tag{1}$$

where *I(x,y)* is the input image, $l = \lfloor x \rfloor$, $k = \lfloor y \rfloor$, and the definition of *dx* and *dy* is $dx = x - l$ and $dy = y - k$, respectively. The cubic weighting function *r(x)* is:

$$r(x) = \frac{1}{6}\left[p(x+2)^3 - 4p(x+1)^3 + 6p(x)^3 - 4p(x-1)^3 \right] \tag{2}$$

where the function *p(x)* has the form

$$p(x) = \begin{cases} x & x > 0 \\ 0 & x \le 0 \end{cases} \tag{3}$$

Full details about down-sampling and bi-cubic interpolation can be found in the work by Zhen *et al.* [15]. The multi-resolution method prepares the vessel wall's edge boundary such that the vessel wall thickness tends to be equivalent to the scale of the Gaussian kernels. This

infrastructure will allow the scale-space based vascular edge segmentation methods applicable to vessel wall for edge detection, which in turn is necessary for locating the carotid artery in the image frame. Note that, this automated method might detect the jugular vein border edges if they are present in the image frame. The current architecture allows a methodology to handle this challenge in case multiple edges are determined during the process of carotid artery recognition. This will be discussed in step 5 (called refinement).

Step 2: Speckle reduction.

Speckle noise was attenuated by using a first-order local statistics filter (named as *lsmv* by the authors [16, 17]), which gave the best performance in the specific case of carotid imaging. Figure 2.C shows the despeckled image. The despeckle filter is useful for avoiding spurious peaks during the distal (far) adventitia identification in subsequent steps. This technique is very well established [16, 17] and gave the authors the optimal results.

Step 3: Far Adventitia recognition.

The despeckled image was filtered by using a first order derivative of a Gaussian kernel with the scale σ and convolving with input image $I(\mathbf{x})$ (being $\mathbf{x}$ is the 2-D vector coordinates (x,y)):

$$F(\mathbf{x},\sigma) = \sigma \cdot I(\mathbf{x}) \otimes \frac{\partial G}{\partial \mathbf{x}}(\mathbf{x},\sigma) \tag{4}$$

where $\frac{\partial G}{\partial \mathbf{x}}$ is the first order derivative of the Gaussian kernel $G(\mathbf{x},\sigma)$ and $F(\mathbf{x},\sigma)$ is the filtered image. The Gaussian kernel , which had size *S* equal to 35x35 pixels, was defined as:

$$G(\mathbf{x},\sigma) = \frac{1}{2\pi\sigma^2} e^{\|\mathbf{x}\|^2/2\sigma^2} \tag{5}$$

In eq. (4), the symbol ' $\cdot$ ' denotes multiplication and the symbol ' $\otimes$ ' denotes convolution.

Figure 2.D shows the results of the filtering by the Gaussian derivative. The scale parameter (σ) of the Gaussian derivative kernel was taken equal to 8 pixels, *i.e.* twice the expected dimension of the IMT value in an original fine resolution image. In fact, an average IMT value of say 1 mm corresponds to about 12-16 pixels in the original image scale and, consequently, to 6-8 pixels in the coarse or down-sampled image. The white horizontal stripes of fig. 2.D are relative to the proximal (near) and distal (far) adventitia layers.

Step 4: Heuristic-Based Automated Far adventitia (AD_F)

Figure 2.E shows the intensity profile of one column (upper edge of the image to lower edge of the image) of the filtered image of fig. 2.D. The proximal and distal walls are intensity maxima saturated to the value of 255. To automatically trace the profile of the distal (far) wall, we used a heuristic search applied to the intensity profile of each column. Starting from the bottom of the image (*i.e.* from the pixel with the higher row index, note that (0,0) is the top left hand corner of the image), we search for the first white region where the width of the region is W_{search} pixels. In fig. 2.D, the white region corresponding to the far adventitia wall has a width of 8 pixels (equal to σ), which is the same size of the Gaussian kernel (as reported in the description of Step 3). Therefore, a threshold value of 6 pixels width was the optimal choice for our database, and ensured the correct identification of the AD_F in all the images. On taking the lower values, it lead to the identification of other structures that were not the far wall; such structures can be present below the carotid far wall (*i.e.* they are usually deeper than the artery and correspond to the neck structures around the trachea). Conversely, higher search region, pixels we could not detect the thinner arteries in our database (*i.e.* the carotids having IMT lower than 05-0.6 mm, typical of healthy and young subjects). Therefore, a search region of W_{search} = 6 pixels width was the optimal choice for our database, and ensured the correct identification of the AD_F in all the images. Figure 2.F shows the final AD_F profiles.

The deepest point of this region (*i.e.* the pixel with the higher row index) marked the position of the far adventitia (AD_F) layer on that column. The sequence of points resulting from the heuristic search for each of the image columns constituted the overall automated AD_F tracing. We followed the concept of decimation of columns as adapted by Rossi *et al.* [18]. They showed that their heuristic search procedure combined with decimation ensured a faster and efficient strategy for carotid detection.

Step 5: AD_F *refinement*.

Pilot studies showed that the traced AD_F profile could be characterized by spikes and false points identification. This could be due to several reasons such as (a) variations in intensities due to variety of reasons such as probe interface with skin, frequency of operation and gain settings; (b) gaps in the media walls due to non-uniformity of the media layer; (c) presence of jugular vein due to orientation scanning; (d) shadow effects due to presence of calcium in the near wall, or combination of these. We have therefore introduced a validation protocol, which provides a check on the AD_F profile ensuring that the location of CA is at correct place and the far adventitia segmentation edge is smooth. This architecture of the validation step refines the AD_F profile and is done in two steps: (a) *refinement using anatomic lumen* and (b) *spike removal*.

- *Step 5.1 – Refinement by anatomic (Lumen) reference.*

  This check has been introduced to avoid error conditions of AD_F profile protruding into the lumen vessel or beyond. Thus, the objective should be to ensure that the far adventitia borders (stage-I output) does not penetrate lumen region (lumen is above the ADF border in the above discussion). We have thus modeled the lumen segmentation region as a classification process with two classes similar to the approach by Molinari *et al.* [8, 19]. The number of classes *K* was set to 50, having interval of 0.02. For detailed discussion on optimization of *K*, readers can see the CULEX strategy for lumen detection by Molinari *et al.* [8, 19]. In previous studies, we showed that pixels belonging to the lumen of the

artery are usually classified into the first few classes of this 2DH [8]. Our validation of automated computer-based lumen pixels recognition was done against manual segmentations. Results revealed that pixels of the lumen have a mean values classified in the first 4 classes and a standard deviation in the first 7 classes. We therefore consider a pixel as possibly belonging to the artery lumen if its neighborhood intensity is lower than 0.08 and if its neighborhood standard deviation is lower than 0.14 [14]. Figure 3 shows the lumen region selection process in four images: fig. 3.A depicts the original image after automatic cropping; fig 3.B depicts the image after speckle noise removal; the 2D histogram (2DH) showing the relationship between the normalized mean and normalized standard deviation can be seen in fig 3.C. The gray region in the 2DH represents what we consider the lumen region of the carotid artery. All the image pixels falling into this region have been depicted in gray in fig 3.D.

We therefore utilize the lumen region as follows. The AD_F points along the CA are considered one by one. For each AD_F point:

1. *Region of Interest Estimation (ROI_{Lumen})*: We consider the sequence of the 30 pixels (ROI_{Lumen}) above it (*i.e.,* the 30 pixels located above the AD_F point, towards the top of the image, and, therefore, with lower row indexes).
2. *Failure of AD_F profile point*: We test if the ROI_L drawn around the AD_F profile points cross the lumen region and have penetrated into the lumen region by at least 15 pixels or more (let's indicate this threshold value by T_{Lumen}). If this does not happen, then the AD_F profile point is considered to have failed the lumen test. Pilot experiments we conducted revealed that suitable values for T_L are comprised between 12 and 20 pixels.
3. *Tagging of Profile Points*: These failed *AD_F profile point*s must not belong to the AD_F boundary. These AD_F points which fail the lumen test are tagged as 0, while

rest of the points are tagged as 1. AD_F All the AD_F points that tagged as 0 are deleted from the AD_F list.

4. The procedure is repeated for each AD_F point along the CA artery.

Table II summarizes all the thresholds and parameters we used in CAMES. Figure 4 reports sample results of lumen test. In figure 4.A the initial AD_F guess is shown by gray squares; fig 4.B shows the AD_F points that passed the lumen test (gray diamonds). Figure 4.C is the down sampled and despeckled image and fig 4.D is the same image with the lumen pixels in white. The white diamonds are the AD_F points that passed the lumen test. Note that even though, the lumen anatomic information, which acts as a reference, provides a good test for catching a series of wrongly computed AD_F boundary, it might slip from sudden bumps which may be due to the changes in grayscale intensity due presence of unusual high intensity in lumen region or a calcium deposit in the near wall causing a shadow in far wall region. This sudden spike can then be easily detected ahead using the spike detection method.

- *Step 5.2 –Spike detection and removal.*

  We implemented an intelligent strategy for spike detection and removal. Basically, we compute the first order derivative of the AD_F profile and check for values higher than T_{Spike} = 15 pixels. This value was chosen empirically by considering the image resolution. When working with images having approximate resolution of about 0.06 mm/pixel, an IMT value of 1 mm would be about 12-16 pixels. Therefore, a jump in the AD_F profile of the same order of magnitude of the IMT value is clearly a spike and error condition. If the spike is at the very beginning of the image (first 10 columns) or at the end (last 10 columns), then the spiky point is simply deleted. We decided to delete spikes at the beginning or end of the image because their correction and substitution with another value would require the moving average with the neighboring points. However, spikes at the beginning or end of the image usually have too few neighboring points to perform a

robust moving average. Therefore, we decided to remove them. Otherwise, all spikes are considered and either substituted by a neighborhood moving average or removed. Figure 5 reports the spike removal procedure for the same image of figure 4. Final AD_F points are represented by gray circles.

Step 6: Up-sampling of far adventitia (AD_F).

The AD_F profile was then up-sampled to the original fine scale and superimposed over the original cropped image (fig. 2.F) for both visualization and determination of the region of interest for segmentation (or calibration) phase (Stage-II). At this stage, the CA far adventitia is automatically located in the image frame thereby providing the guidance zone for the automated border segmentation.

B.2 *Stage-II: Domain-Based LI/MA Segmentation Strategy*

Stage-II is focused narrowly in the region of interest, where the objective is to estimate the LI/MA borders accurately. Here we model a filter in the guidance zone, such that the operation allows for acting as a high pass filter enhancing the intensity edges. For ultrasound images, such a filter can be thought as a First Order Absolute Moment (FOAM). These filtered edges are then heuristically captured to build the LI and MA segmentation borders in the far wall of the carotid artery in the image frame. Stage-II is sub-divided into three steps as follows:

Step 1: Creation of the Guidance Zone.

We built a region-of-interest (ROI) or guidance zone (GZ) around the automatically traced *far adventitia* AD_F profile, so called the domain region in which pixel processing was done to estimate LI and MA borders. Note that the GZ must have a region whose envelope length is at least same length as the width of the AD_F curve along the carotid artery. From the database, we observed that the average internal diameter of the human common carotid artery is 6 mm [20],

which corresponds to be about 100 pixels. Since the total wall thickness for the near and far wall when combined is around 30 pixels (we called this as GZ_{height}) which comes to one-third of the lumen diameter, we therefore decided to keep the envelope's GZ_{height} to be around $1/3^{rd}$ the lumen diameter. Figure 6.A shows the GZ (depicted in the original image scale of fine resolution).

Step 2: Edge Enhancement Gradient of Gaussian (GoG) Filtering: FOAM Operator.

We used the ***F**irst **O**rder **A**bsolute **M**oment* (FOAM) operator for final segmentation of LI and MA borders in the automatically designed guidance zone obtained from the multi-resolution approach. The FOAM operator is a regularized edge-based operator, was first introduced by Demi *et al.* [21] and then extended by Faita *et al*. [4] for an accurate semi-automated IMT measurement in ultrasound images.

Considering an image $I(x,y)$ and two circular domains having radiuses equal to θ_1 and θ_2, respectively, the FOAM edge $e(x,y)$ operator is mathematically defined as:

$$e(x,y) = \iint_{\theta_2} \left| I_1(x,y) - I(x-k, y-l) \right| \cdot G(k,l,\sigma_3)\ dk\ dl \qquad (6)$$

where $I_1(x,y) = \iint_{\theta_1} I(x-k, y-l) \cdot G(x,y,\sigma_1)\ dk\ dl$ and is computed by low-pass filtering the input image by a Gaussian kernel with standard deviations equal to σ_1 and domain region equal to θ_1. The FOAM operator represents the spatial distribution of the variability of the intensity levels of the points in the domain θ_2 with respect to the average of the domain θ_1 [22], with a regularization Gaussian kernel with standard deviation equal to σ_3. Therefore, in homogeneous regions (*i.e.* in regions without intensity changes and that are of the same gray level), the FOAM edge value is close to zero. When computed in proximity of an intensity gradient, the FOAM edge value rises to a maximum. Gemignani *et al.* [22] optimized the values of θ_1 and θ_2 for ultrasound vascular images and suggested to link the Gaussian Kernel sizes to

the image resolution [22]. Also, they suggested using all the σ values equal to 1/3rd of the kernel size. This ensured optimized representation of the intensity discontinuities (*i.e.* in this specific case, of the interfaces between the carotid layers).

Recently, Faita *et al*. showed that better robustness to noise can be achieved by adopting a third Gaussian Kernel function and proposed adopting the following definition of FOAM [4]:

$$e(x,y)=\iint_{\theta_2}\left| I_1(x,y)-I_2(x-k,y-l)\right|\cdot G(k,l,\sigma_3)\,dk\;dl \qquad (7)$$

where $I_1(x,y)=\iint_{\theta_1} I(x-k,y-l)\cdot G(x,y,\sigma_1)\,dk\;dl$ and

$I_2(x,y)=\iint_{\theta_2} I(x-k,y-l)\cdot G(x,y,\sigma_2)\,dk\;dl$ are computed by low-pass filtering the input image by a Gaussian kernel with standard deviations equal to σ_1 and σ_2, respectively. The use of two different apertures values σ_1 and σ_2 implements a filter that is similar to the *Gradient-of-Gaussians* (GoG) filter, which is a high-pass filter, enhancing the intensity edges. The regularization term $G(x,y,\sigma_3)$ is Gaussian filter with standard deviation equal to σ_3.

We linked the Gaussian Kernel sizes and σ values to the image conversion factor (the best conversion factor was τ_{Nicosia} = 0.06 mm/pixel, as reported by Table I), and chose the value of η_{MRAFOAM} = 0.3 mm as pixel conversion factor for the FOAM operator in the multi-resolution framework (MRFOAM). Hence, we used the kernel size $\theta_1 = \theta_3 = \eta_{\text{MRAFOAM}} / \tau_{\text{Nicosia}}$. This yields, $\theta_1 = \theta_3$ = 0.3/0.06 = 5 pixels. As suggested by Faita *et al.* [4], we took $\theta_2 = 2\theta_1$ = 10 pixels. The Gaussian Kernel parameters were then taken equal to $\sigma_1 = \sigma_3 = \lceil \theta_1 / 3 \rceil = 2$ pixels and $\sigma_2 = \lceil \theta_2 / 3 \rceil = 3$ pixels.

Table II summarizes the parameters we used in our CAMES technique. The value of 0.3 mm value was similar to that adopted by Faita *et al.*, who used a value of 0.28 mm (see [4]). We observed that higher values originated larger Gaussian Kernels, which decreased the accuracy of the LI/MA representation and, therefore, decreased the FOAM localization performance. Conversely, values lower than 0.3 mm originated very small Gaussian Kernels, which did not ensure sufficient noise robustness.

Step 3: Heuristic Approach for LI/MA Borders.

The LI/MA edge interfaces in the GZ were then searched by relying on heuristic search. This can be explained much better in the following way: Figure 6.C shows the intensity profile of a column of the FOAM operator in fig. 6.B. The LI and MA transitions produce two high-intensity peaks on the FOAM column profile and we model these peaks as 90^{th} percentile of the distribution along that column. First peak is MA and second peak is LI.

We continue the search ahead in the direction of the decreasing row index (*i.e.,* towards the top or proximal wall of the image) and again the location is searched which reflects 90^{th} percentile of the intensity distribution, marked as the LI interface. This procedure is repeated column-by-column along the CA artery until all the points along the AD_F curve are examined. If one of the two maxima's is not found, that column is discarded.

A subsequent outlier removal step cleans disconnected columns and regularizes the profiles, ensuring the constraint that a maximal distance between LI and MA is lower than 2 mm. The constraint of 2 mm is consistent with the IMT value (which is lower than 1 mm for healthy adults) even in the case of pathologic vessels with increased wall thickness [23]. An IMT value higher than 2 mm can be found only in vessels with the beginning of plaque build-up. This regularization step ensures an optimal representation of the LI/MA profiles in healthy arteries or in arteries with increased IMT, but it is not suited to plaque analysis.

III. Results

We show the results of the CAMES Vs. CALEX on the 365 image database. We do not compare CAMES with FOAM directly, since FOAM is not an automated technique and requires manual ROI selection. According to previous studies [18, 24, 25], we defined the CA as correctly recognized in the image frame if the distance between the automated tracing of the AD_F and the manually traced MA boundary was lower than 2 mm (which is a value about twice that of the average IMT). CAMES correctly identified the CA in all the 365 images of the dataset, showing 100% accuracy. This is a first time in the history a computer-based technique can recognize the carotid artery automatically. CALEX could not correctly identify the CA in 12 images out of 365, having a failure rate of 3.3 %.

A. Distal Wall Segmentation and Performance

Table III reports the overall LI (first row) and MA (second row) segmentation errors for the CAMES (first column) and CALEX (second column) techniques. CAMES outperformed CALEX in both LI and MA tracings, leading to an improvement of the distal wall segmentation error equal to 8 % for LI and 42 % for MA. The average LI and MA segmentation errors using CAMES were 0.081 ± 0.099 mm and 0.082 ± 0.197 mm, respectively.

The Percent Statistic Test [26] indicated that CAMES profiles could be considered as equivalent to manually traced ones. Considering n=3 and N=365; we obtained p=0.5 and θ=0.051. Therefore, considering $\alpha = 0.05$, the Percent Statistic Test is passed when $Z_0 > 0.448$ (see [26] for details about the Percent Statistic Test). CAMES showed Z_0 scores equal to 0.545 (for the LI interface) and of 0.530 (for the MA interface), while CALEX showed Z_0 scores of 0.478 (LI) and 0.451 (MA).

B. IMT Measurement Bias

The third row of Table III reports the IMT measurement bias. CAMES showed a measurement error significantly lower than CALEX (*Student's t-test,* $p<10^{-3}$): CAMES error was as low as 0.078 ± 0.112 mm, whereas CALEX showed a higher error equal to 0.121 ± 0.334 mm. CAMES showed an improvement over CALEX by 36%. Table IV reports the IMT value measured by CAMES (first column), CALEX (second column) and ground-truth (*GT* – third column). It can be noticed that CAMES demonstrated a very accurate IMT computation equal to 0.91 ± 0.45 mm, which is very close to ground-truth of 0.95 ± 0.41 mm. On the contrary, CALEX measurement was less accurate resulting in the IMT value of 0.83 ± 0.39 mm. On the overall, both the techniques under-estimated IMTs.

Another way of interpretation is by computing the figure-of-merit (FoM) in % as:

$$FoM_{CAMES} = 100 - \frac{\overline{GT}_{IMT} - \overline{CAMES}_{IMT}}{\overline{GT}_{IMT}} \cdot 100$$
$$FoM_{CALEX} = 100 - \frac{\overline{GT}_{IMT} - \overline{CALEX}_{IMT}}{\overline{GT}_{IMT}} \cdot 100 \quad (8)$$

Using the above definitions, the FoM for CALEX came out to be 87.4%, while CAMES was much superior yielding to 95.8%. This clearly demonstrates the how close and reproducible the IMTs are with CAMES compared to CALEX.

Figure 7 reports the scatter diagrams showing the CALEX (on the left) and CAMES (on the right) IMT estimates with respect to GT. CAMES showed a correlation coefficient as high as 0.90 (95% C.I. = 0.88 – 0.92), whereas the correlation coefficient of CALEX was only of 0.64 (95% C.I. = 0.58 – 0.70).

Figure 8 shows the Bland-Altmann plots for CALEX (left) and CAMES (right). Clearly, CAMES estimates are more accurate than CALEX.

The standard deviation of the IMT bias (*i.e.* the reproducibility) is equal to 0.122 mm for CAMES and 0.334 mm for CALEX. This is partly due to the anatomical differences of the

subjects in our database, which comprised healthy and pathological subjects. Part of the variability was also due to the differences between the three operators: the first operator measured an IMT value equal to 0.93±0.38 mm, the second 0.96±0.37 mm, and the third 0.96±0.41 mm. Hence, operator variability affected the overall reproducibility, even though the principal source of variability remains the difference among subjects.

IV. Discussion

The aim of this paper was to develop an automated multi-resolution recognition and edge-based segmentation system for high-performance IMT measurement in longitudinal ultrasound B-mode carotid imaging.

We benchmarked the system with recently published standardized system based on an integrated approach of feature extraction and classification (called CALEX*)* and showed an improvement of LI and MA interfaces by 8% and 42%, respectively, while the IMT measurement bias decreased by 36%. The overall Figure of Merit (FoM) of CAMES was 95.8%.

Complete automation is a major advantage of this technique. The CA is automatically located in the image frame by a processing strategy based on multi-resolution analysis. By fine to coarse sampling the image, we lessen the computational burden, yet maintaining accuracy in the far adventitia wall tracing. The advantage of using a multi-resolution approach with respect to other automated techniques for CA recognition (*i.e.* local statistics [14], integrated approach [10], Hough transform [27], parametrical template matching applied to the radio-frequency signal [18]) is the possibility of obtaining a clear visualization of the walls (fig. 2.D) with a very reduced computational burden and high robustness to noise. Our stage-I system provides a check based on anatomic information such as lumen, which allows full robustness to the system for CA recognition.

The segmentation in stage-II was performed by using the FOAM edge operator, which is conceptually similar to a Gaussian of Gradient (GoG)-based technique incorporating speckle noise reduction and high-sensitivity to gray levels changes. Faita *et al.* showed that FOAM operator is very effective in detecting the position of the LI and MA interfaces; in their study, they documented a IMT measurement error as low as 0.01 mm, with best performance reaching errors of about 0.001 mm [4]. Another edge-based technique was published by Stein *et al.* [6] in 2005. They developed a user-driven computer method for aiding IMT measurement where the user had to place a ROI around the far adventitia wall, and the program computed the image gradients. IMT was measured as distance between the two highest gradient peaks. They obtained average IMT measurement errors equal to 0.012 ± 0.006 mm. In a recent extensive review about the computer methods for carotid segmentation and IMT measurement from ultrasound images, we showed that gradient-based methods are the best performing techniques [2]. High performance and fast computation made the Gaussian gradient-based LI and MA detection the best choice for CAMES, when used under scale-space framework in multi-resolution paradigm.

Overall CAMES system performance in terms of LI and MA tracing accuracy were very encouraging. First, CAMES tracings differed from manual tracings as much as manual tracings of different operators differed among them (Percent Statistic Test). Then, tracing errors could be considered in line with the best performing techniques (including user-driven ones) we could find in the literature. In 2009, Destrempes *et al.* [28] proposed a segmentation strategy based on Nakagami modeling of the intensities of the artery lumen, and of the intima, media, and adventitia layers. They documented tracing errors equal to 0.021 ± 0.013 mm for LI and 0.016 ± 0.007 mm for MA. These are the lowest errors we could find in literature. Despite higher LI and MA tracing biases, CAMES showed three major advantages when compared to Destrempes's technique. First, the methodology based on Nakagami modeling requires extensive tuning and training of the system. This implies that the computational cost is relatively high and that the system development procedure is long. Second, specific training and tuning is required in order to

optimize performance on a specific scanner. If different scanners acquired the images, then re-training and re-tuning would be mandatory. Hence, this methodology would not be optimal for large multi-centre studies and real time clinical environments. Third, the technique by Destrempes is not automated, since user interaction is required for selecting the optimal wall portion during the modeling process.

Figure 9 shows samples of CAMES segmentation. Figures 9.A, 9.C, and 9.E report the LI automated tracings of CAMES (white line) in comparison to GT (white dashed line) with grayscale cropped image in background; fig. 9.B, 9.D, and 9.F report the MA tracings (black line) in comparison to GT (black dashed line).

In Stage-I, CAMES correctly processed all the 365 images of the database by tracing the AD_F profile, showing a success rate of 100%. This percentage drops to 96% if the *refinement by anatomic reference (Lumen)* is omitted. This check is very important in Stage-I, since it increases the recognition accuracy and makes the system insensitive to noise and variability. By recognition accuracy we mean that instead of CA, JV could be detected. Figure 1.D shows that the lumen identification procedure also detects the pixels belonging to the jugular vein (JV). This is correct behavior, since the pixels of the JV lumen have same characteristics of those of the CA lumen. However, this is not an error condition. In fact, the lumen is used only for the validation of the AD_F point, and not for their tracing. This means that if a candidate AD_F point fails the *refinement by anatomic reference (lumen) check*, it is not part of the AD_F curve. No points are added to the AD_F profile by the *anatomic reference (lumen) check* procedure. Therefore, the presence of the lumen points of the JV does not constitute an error condition for our technique. The JV was present in 66% of the images of our database and it was always recognized; however, this did not cause any tracing obstruction for far adventitia border detection and carotid artery recognition.

In our recent review, we showed that snake-based segmentation techniques could provide very accurate results whereby, the LI and MA segmentation errors equal to about 0.035 ± 0.032

mm and 0.037 ± 0.029 mm, respectively [2, 11]. Clearly, the snake-based technique outperformed CAMES.

However, CAMES has some major advantages over snake-based procedures are. CAMES does not require any tuning or parameter optimization. Table II reports all the parameters we set and used in CAMES, particularly in Stage-II where we used FOAM. Actually, all the parameters are dependent on the conversion factor, which is reported by the first row and which determines all the other parameters. According to previous studies, we used a value of 0.3 mm. This value is an optimal compromise between the need for accurate localization of the LI/MA interfaces, and robustness to noise. If this value decreases, the localization of the LI/MA interfaces becomes more accurate, but the FOAM operator becomes noisy, since the Gaussian Kernels become too small to ensure noise attenuation. Conversely, if the conversion factor is greater than 0.35 mm, the Gaussian Kernels become larger. In this condition, CAMES becomes very robust with respect to noise, but the LI/MA representation is less accurate. In fact, larger Gaussian Kernels cause a higher blurring on the LI/MA interfaces representation. We found that the value of 0.3 mm was suitable for all the images of the database, even if they had a different resolution. Conversely, snakes performance is very dependent on the rigidity and elasticity parameters. Fine-tuning of the parameters helps obtaining high performance, but reduces applicability to diversity in the image data set due to gain settings taken by different set of sonographers.

CAMES implementation is low in computation and is very fast. CAMES provides LI and MA tracings and IMT measurement in less than 15 seconds. Snake-based techniques require several iterations until the curve converges to the LI or MA boundary. Hence, computational time is usually of about 20-30 seconds.

Table II summarizes the parameters used in CAMES system. The table has two sets of parameters, those used for stage-I and stage-II, respectively. The table has three columns: first column shows the parameter and its symbols, column two shows the values the parameter can takes, while the last column is the safe range of the parameter. The CAMES parameters related to

stage-I are (i) Size (S) of the Gaussian Kernel size; (ii) Scale Parameter (σ), (iii) width of the AD_F search region (W_{search}); (iv) pixels neighborhood size (*WIN*), (v) number of classes (*K*) of the 2DH, (vi) ROI width for lumen validation (ROI_{Lumen}), (vii) Lumen test failure threshold (T_{Lumen}) and (viii) Spike detection threshold (T_{Spike}). For a 100% success of stage-I of the CAMES system, the best combination of parameters for stage-I were: S equal to 35 pixels; σ ranged between 6 to 10 pixels, W_{search} equal to 6 pixels; *WIN* was 10x10 wide, *K* was equal to 20 classes, T_{Spike} ranged 12-16 pixels, ROI_{Lumen} and (T_{Lumen}) set to 30 and 15 pixels, respectively. The sensitivity of AD_F detection would change if ROI_{Lumen} and T_{Lumen} is set greater than 30 and lower than 15 pixels, respectively. This would cause about 10% of the image database to fail stage-I.

Stage-II set of parameters were: MRFOAM Calibration Factor (η_{MRFOAM}), Gaussian Kernel sizes: $\theta_1, \theta_2, \theta_3$ and Gaussian scale $\sigma_1, \sigma_2, \sigma_3$. Note that Gaussian Kernel sizes: $\theta_1, \theta_2, \theta_3$ are function of η_{MRFOAM} and Gaussian scales $\sigma_1, \sigma_2, \sigma_3$ are function of Gaussian Kernel sizes: $\theta_1, \theta_2, \theta_3$. Thus there was a dependency of Gaussian Kernel sizes and Gaussian scales on MRFOAM Calibration Factor (η_{MRFOAM}). This parameter was set to 0.3 mm. The effect of increasing η_{MRFOAM} was over smoothing LI/MA peaks in the MRAFOAM edge map, which would preclude the accurate LI/MA peak detection increasing the overall system error. Conversely, a lower η_{MRFOAM} value caused a noisy FOAM representation, thus originating LI/MA profiles characterized by variability and ripple. Thus the most stable and safe value for η_{MRFOAM} was set to 0.3 mm made the stage-II completely stable with FoM factor reaching to 95.8%. Lastly, we would like to remark that the values shown in the middle column for the table II were exactly used for all 365 images of the database. We do however believe that, a very large database (reaching above 5000 images or above) and cohort studies would completely validate our entire system to full proof. We however validated our system sensitivity with variations in parameters and further benchmarking with CALEX system.

Overall, the average processing time for CAMES was less than 15 s, while CALEX required 3 s [11]. Suri and his team (at Global Biomedical Technologies, Inc.) recently ported the system in Windows OS environment using C++ under Visual Studio (called AtheroEdge™), obtaining computational costs lower than 1 s per image without refinement check. Work is currently active to actually design a platform independent system with GPU settings to make it real time.

V. Conclusion

In conclusion, CAMES brought automation in carotid wall segmentation and IMT measurement based on edge detection strategy. Among all possible techniques for automated carotid artery location, we introduced a multi-resolution approach, which ensured accuracy and real-time computation. Compared to previously developed techniques (based on integrated approach [10] or local statistics [8]), multi-resolution required less than 1 s (with respect to 3 s of integrated approach [10] and about 30 s of local statistics [8]). Accuracy increased with respect to a previously developed automated technique (CALEX). Specifically, the IMT measurement FoM improved from 83% to about 94%. Real-time computation, robustness to noise, and complete automation, make CAMES a suitable and validated clinical tool for automating and improving IMT measurement in multi-center large clinical trials.

Acknowledgements

The Authors would like to thank Dr. William Liboni from the Neurology Division of the Gradenigo Hospital of Torino (Italy) and Dr. Rui Rocha from INEB – Inst. de Eng. Biomédica, Divisão de Sinal e Imagem of Porto (Portugal) for providing the ultrasound images.

References

[1] I. M. van der Meer, M. L. Bots, A. Hofman, A. I. del Sol, D. A. van der Kuip, and J. C. Witteman, "Predictive value of noninvasive measures of atherosclerosis for incident myocardial infarction: the Rotterdam Study," *Circulation,* vol. 109, no. 9, pp. 1089-94, Mar 9, 2004.

[2] F. Molinari, G. Zeng, and J. S. Suri, "A state of the art review on intima-media thickness (IMT) measurement and wall segmentation techniques for carotid ultrasound," *Computer Methods and Programs in Biomedicine,* vol. 100, pp. 201-221, 2010.

[3] E. de Groot, S. I. van Leuven, R. Duivenvoorden, M. C. Meuwese, F. Akdim, M. L. Bots, and J. J. Kastelein, "Measurement of carotid intima-media thickness to assess progression and regression of atherosclerosis," *Nat Clin Pract Cardiovasc Med,* vol. 5, no. 5, pp. 280-8, May, 2008.

[4] F. Faita, V. Gemignani, E. Bianchini, C. Giannarelli, L. Ghiadoni, and M. Demi, "Real-time measurement system for evaluation of the carotid intima-media thickness with a robust edge operator," *J Ultrasound Med,* vol. 27, no. 9, pp. 1353-61, Sep, 2008.

[5] C. Liguori, A. Paolillo, and A. Pietrosanto, "An automatic measurement system for the evaluation of carotid intima-media thickness," *Instrumentation and Measurement, IEEE Transactions on,* vol. 50, no. 6, pp. 1684-1691, 2001.

[6] J. H. Stein, C. E. Korcarz, M. E. Mays, P. S. Douglas, M. Palta, H. Zhang, T. Lecaire, D. Paine, D. Gustafson, and L. Fan, "A semiautomated ultrasound border detection program that facilitates clinical measurement of ultrasound carotid intima-media thickness," *J Am Soc Echocardiogr,* vol. 18, no. 3, pp. 244-51, Mar, 2005.

[7] D. C. Cheng, A. Schmidt-Trucksass, K. S. Cheng, and H. Burkhardt, "Using snakes to detect the intimal and adventitial layers of the common carotid artery wall in sonographic images," *Comput Methods Programs Biomed,* vol. 67, no. 1, pp. 27-37, Jan, 2002.

[8] S. Delsanto, F. Molinari, P. Giustetto, W. Liboni, S. Badalamenti, and J. S. Suri, "Characterization of a Completely User-Independent Algorithm for Carotid Artery Segmentation in 2-D Ultrasound Images," *Instrumentation and Measurement, IEEE Transactions on,* vol. 56, no. 4, pp. 1265-1274, 2007.

[9] C. P. Loizou, C. S. Pattichis, M. Pantziaris, T. Tyllis, and A. Nicolaides, "Snakes based segmentation of the common carotid artery intima media," *Med Biol Eng Comput,* vol. 45, no. 1, pp. 35-49, Jan, 2007.

[10] F. Molinari, G. Zeng, and J. S. Suri, "An integrated approach to computer- based automated tracing and its validation for 200 common carotid arterial wall ultrasound images: A new technique," *J Ultras Med,* vol. 29, pp. 399-418, 2010.

[11] F. Molinari, G. Zeng, and J. S. Suri, "Intima-media thickness: setting a standard for completely automated method for ultrasound," *IEEE Transaction on Ultrasonics Ferroelectrics and Frequency Control,* vol. 57, no. 5, pp. 1112-1124, 2010.

[12] E. Kyriacou, M. S. Pattichis, C. I. Christodoulou, C. S. Pattichis, S. Kakkos, G. M., and A. Nicolaides, "Ultrasound imaging in the analysis of carotid plaque morphology for the assessment of stroke," *Plaque imaging: pixel to molecular level*, J. S. Suri, C. Yuan, D. L. Wilson and S. Laxminarayan, eds., pp. 241-275, Amsterdam: IOS Press, 2005.

[13] E. C. Kyriacou, C. S. Pattichis, M. A. Karaolis, C. P. Loizou, C. I. Christodoulou, M. S. Pattichis, S. Kakkos, and A. Nicolaides, "An Integrated System for Assessing Stroke Risk," *Engineering in Medicine and Biology Magazine, IEEE,* vol. 26, no. 5, pp. 43-50, 2007.

[14] F. Molinari, W. Liboni, P. Giustetto, S. Badalamenti, and J. S. Suri, "Automatic computer-based tracings (ACT) in longitudinal 2-D ultrasound images using different scanners," *Journal of Mechanics in Medicine and Biology,* vol. 9, no. 4, pp. 481-505, 2009.

[15] Y. Zhen, S. Jasjit, S. Yajie, and R. Janer, "Four image interpolation techniques for ultrasound breast phantom data acquired using Fischer's full field digital mammography and ultrasound system (FFDMUS): a comparative approach." pp. II-1238-41.

[16] C. P. Loizou, C. S. Pattichis, C. I. Christodoulou, R. S. H. Istepanian, M. Pantziaris, and A. Nicolaides, "Comparative evaluation of despeckle filtering in ultrasound imaging of the carotid artery," *Ultrasonics, Ferroelectrics and Frequency Control, IEEE Transactions on,* vol. 52, no. 10, pp. 1653-1669, 2005.

[17] C. P. Loizou, C. S. Pattichis, M. Pantziaris, T. Tyllis, and A. Nicolaides, "Quality evaluation of ultrasound imaging in the carotid artery based on normalization and speckle reduction filtering," *Med Biol Eng Comput,* vol. 44, no. 5, pp. 414-26, May, 2006.

[18] A. C. Rossi, P. J. Brands, and A. P. Hoeks, "Automatic recognition of the common carotid artery in longitudinal ultrasound B-mode scans," *Med Image Anal,* vol. 12, no. 6, pp. 653-65, Dec, 2008.

[19] F. Molinari, S. Delsanto, P. Giustetto, W. Liboni, S. Badalamenti, and J. S. Suri, "User-independent plaque segmentation and accurate intima-media thickness measurement of carotid artery wall using ultrasound," *Advances in diagnostic and therapeutic ultrasound imaging*, J. S. Suri, C. Kathuria, R. F. Chang, F. Molinari and A. Fenster, eds., pp. 111-140, Norwood, MA: Artech House, 2008.

[20] J. F. Polak, R. A. Kronmal, G. S. Tell, D. H. O'Leary, P. J. Savage, J. M. Gardin, G. H. Rutan, and N. O. Borhani, "Compensatory increase in common carotid artery diameter. Relation to blood pressure and artery intima-media thickness in older adults. Cardiovascular Health Study," *Stroke,* vol. 27, no. 11, pp. 2012-5, Nov, 1996.

[21] M. Demi, M. Paterni, and A. Benassi, "The first absolute central moment in low-level image processing," *Computer Vision and Image Understanding,* vol. 80, no. 1, pp. 57-87, OCT, 2000.

[22] V. Gemignani, F. Faita, L. Ghiadoni, E. Poggianti, and M. Demi, "A system for real-time measurement of the brachial artery diameter in B-mode ultrasound images," *IEEE Trans Med Imaging,* vol. 26, no. 3, pp. 393-404, Mar, 2007.

[23] J. F. Polak, M. J. Pencina, A. Meisner, K. M. Pencina, L. S. Brown, P. A. Wolf, and R. B. D'Agostino, Sr., "Associations of Carotid Artery Intima-Media

Thickness (IMT) With Risk Factors and Prevalent Cardiovascular Disease: Comparison of Mean Common Carotid Artery IMT With Maximum Internal Carotid Artery IMT," *J Ultrasound Med,* vol. 29, no. 12, pp. 1759-68, Dec.
[24] R. Rocha, A. Campilho, J. Silva, E. Azevedo, and R. Santos, "Segmentation of ultrasound images of the carotid using RANSAC and cubic splines," *Comput Methods Programs Biomed*, Jun 14.
[25] R. Rocha, A. Campilho, J. Silva, E. Azevedo, and R. Santos, "Segmentation of the carotid intima-media region in B-Mode ultrasound images," *Image and Vision Computing,* vol. 28, no. 4, pp. 614-625, 2010.
[26] V. Chalana, and Y. Kim, "A methodology for evaluation of boundary detection algorithms on medical images," *IEEE Trans Med Imaging,* vol. 16, no. 5, pp. 642-52, Oct, 1997.
[27] S. Golemati, J. Stoitsis, E. G. Sifakis, T. Balkizas, and K. S. Nikita, "Using the Hough transform to segment ultrasound images of longitudinal and transverse sections of the carotid artery," *Ultrasound Med Biol,* vol. 33, no. 12, pp. 1918-32, Dec, 2007.
[28] F. Destrempes, J. Meunier, M. F. Giroux, G. Soulez, and G. Cloutier, "Segmentation in ultrasonic B-mode images of healthy carotid arteries using mixtures of Nakagami distributions and stochastic optimization," *IEEE Trans Med Imaging,* vol. 28, no. 2, pp. 215-29, Feb, 2009.

Table I – Image Database and Patient Demographics

Characteristics of the image dataset coming for four different Institutions and relative patient demographics. The first column reports the institution, the second the number of image, the third the conversion factor, the fourth the scanner used. Finally, the last two columns report the number of patients and their demographics.

Institution	**Total Images (N)**	**Conversion Factor (τ) (mm/pixel)**	**Ultrasound scanner**	**Patients**	**Age**
Torino (Italy)	200	$\tau_{\text{Torino}} = 0.0625$	ATL HDI5000	150	69 ± 16 years (50-83 years)
Nicosia (Cyprus)	100	$\tau_{\text{Nicosia}} = 0.0600$	ATL HDI3000	100	54 ± 24 years (25-95 years)
Porto	23	$\tau_{\text{Porto}} = 0.0900$	ATL HDI5000	23	[Not published]

(Portugal)					[24, 25]
Cagliari (Italy)	42	$\tau_{Cagliari} = 0.0789$	Esaote MyLab 70	21	68 ± 8 years (59-81 years)

Table II – CAMES *parameters*

CAMES parameters and experimental values used.

Parameter	Value	Experimental Range and Effect
Stage-I (AD_F Identification)		
Gaussian Kernel size (S)	35 pixels	S = 35x35 pixels. Size of the Gaussian Kernel used during stage I process.
Scale Parameter (σ)	8 pixels	σ = 6-10 pixels. Scale of the 1st order Gaussian Kernel derivative during the stage I process.
Width of the AD_F white region (W_{search})	6 pixels	W_{search} = 6 pixels. Width of the white region for the AD_F detection.
Number of classes of 2DH (K)	50	K = 50. Number of classes for the discretization of the normalized mean and standard deviation of the pixel neighborhood. Each class has 0.02 width.
ROI width for lumen validation (ROI_{Lumen})	30 pixels	Sequence of points above AD_F to check for lumen test.
Lumen test failure threshold (T_{Lumen})	15 pixels	Threshold for passing the lumen test.
Spike detection threshold (T_{Spike})	15 pixels	T_{Spike} = 12-16 pixels.

		Determines the difference between consecutive points of a profile that we consider a spike.
Stage II (LI/MA segmentation)		
Height of the Guidance Zone (GZ_{height})	30 pixels	GZ_{height} = 30 pixels. Height of the GZ, which was taken equal to 1/3rd of the lumen diameter.
MRFOAM Calibration Factor (η_{MRFOAM})	0.3 mm	Determines noise robustness and LI/MA accuracy.
Gaussian Kernel size (θ_1)	5 pixels	$\theta_1 = \eta_{MRFOAM} / \tau_{Nicosia}$ Implements the GoG filter. ($\tau_{Nicosia}$ is the conversion factor of Table I)
Gaussian Kernel size (θ_2)	10 pixels	$\theta_2 = 2\theta_1$ Implements the GoG filter
Gaussian Kernel size (θ_3)	5 pixels	$\theta_3 = \eta_{MRFOAM} / \tau_{Nicosia}$ Regularization parameter. ($\tau_{Nicosia}$ is the conversion factor of Table I)
Gaussian scale σ_1 and σ_3 Gaussian scale σ_2	2 pixels 3 pixels	$\sigma_i = \lceil \theta_i / 3 \rceil$

Table III – Performance and Benchmarking

Overall system performance for CAMES (first column) and CALEX (second column).

	CAMES	**CALEX**	**Error reduction**
LI Error ($\overline{\varepsilon}_{LI}$)	0.081 ± 0.099 mm	0.088 ± 0.132 mm	8 %

MA Error ($\bar{\varepsilon}_{MA}$)	0.082 ± 0.197 mm	0.141 ± 0.201 mm	42 %
IMT Bias ($\bar{\mu}$)	0.078 ± 0.112 mm	0.121 ± 0.334 mm	36 %

Table IV – Average IMT and Figure of Merit (FoM)

Average IMT value by CAMES (first column) and CALEX (second column), as compared to ground-truth (third column). The second row reports the figure-of-merit (FoM).

	CAMES	**CALEX**	**Ground-Truth**
IMT measurement	0.91 ± 0.44 mm	0.83 ± 0.39 mm	0.95 ± 0.39 mm
FoM	95.8 %	87.4 %	-

Figure Legends

Figure 1

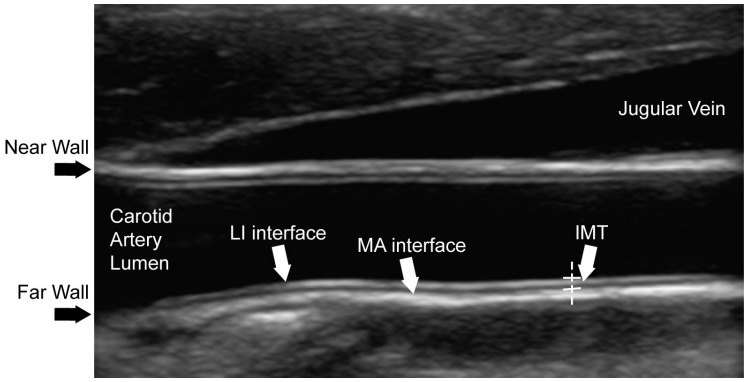

Reference anatomy of a longitudinal ultrasound image of a carotid artery showing the lumen – intima (LI), the media – adventitia (MA) interfaces, and the intima-media thickness (IMT).

Figure 2

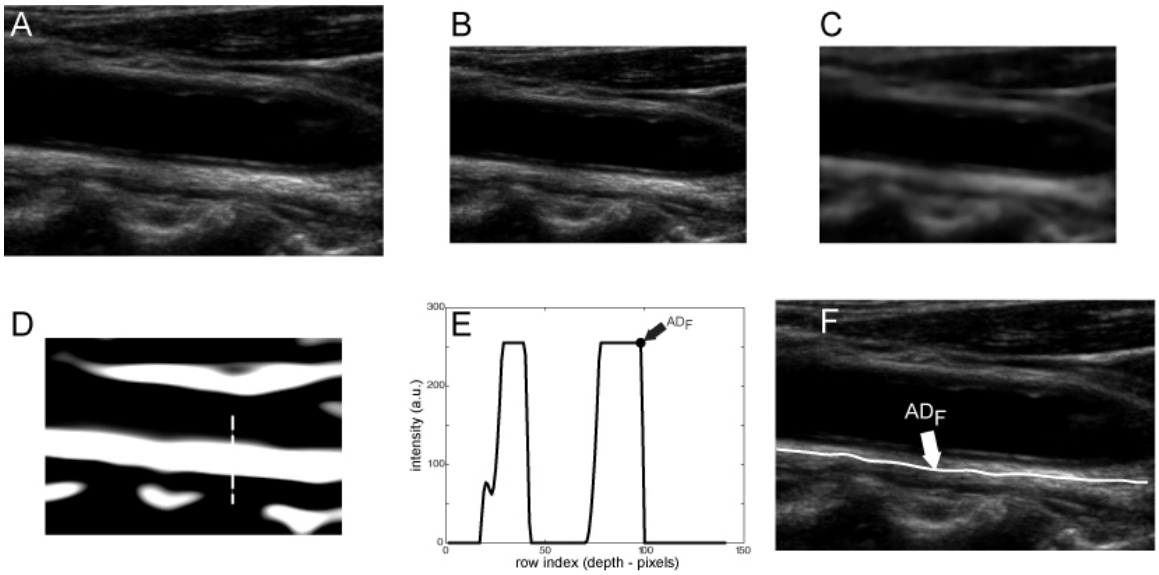

A) Original cropped image. B) Donwsampled image. C) Despeckled image. D) Image after convolution with first-order Gaussian derivative (sigma = 8). E) Intensity profile of the column indicated by the vertical dashed line in panel D. (AD_F indicates the position of the far adventitia wall). F) Cropped image with far adventitia profile overlaid.

Figure 3

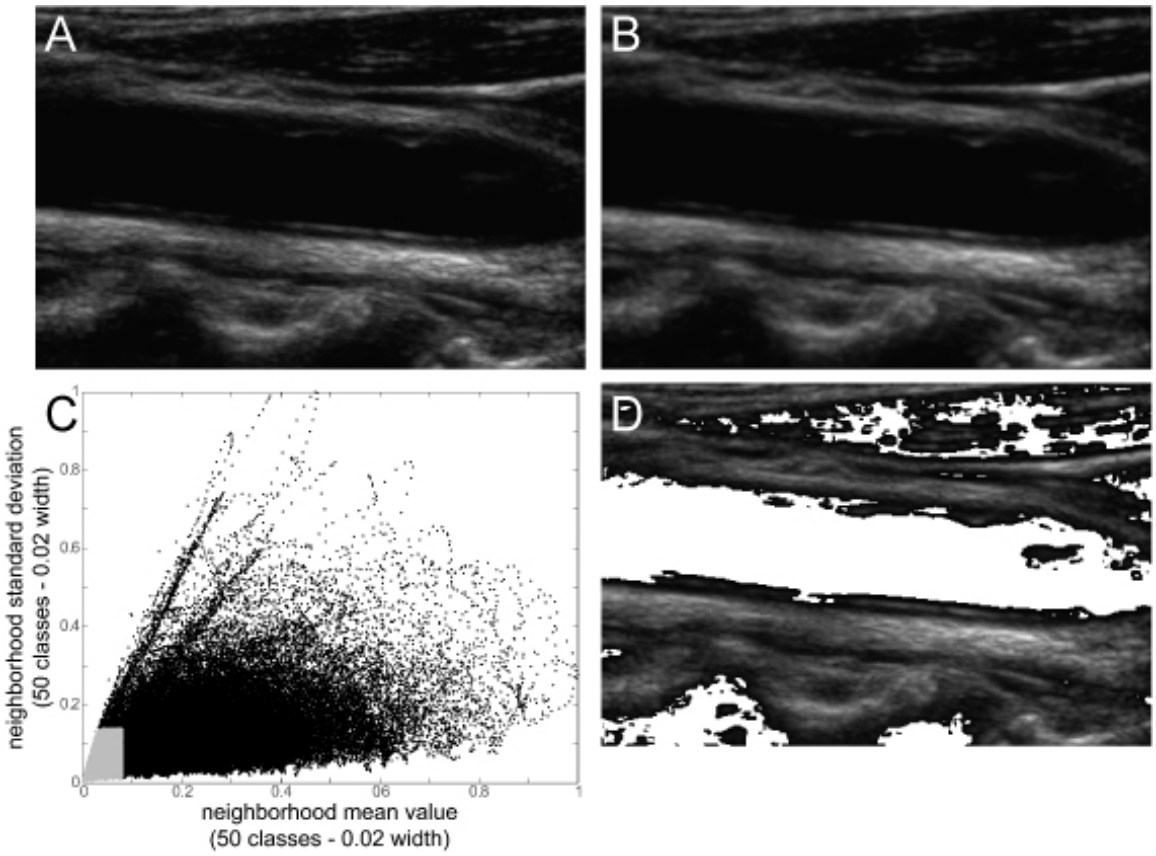

A) Original B-Mode longitudinal image. B) Low-passed filtered image. C) 2DH showing in gray the histogram area where we hypothesize the lumen points should concentrate and in black all the other pixels. D) Lumen points (in white) overlaid to the original B-Mode image of panel A.

Figure 4

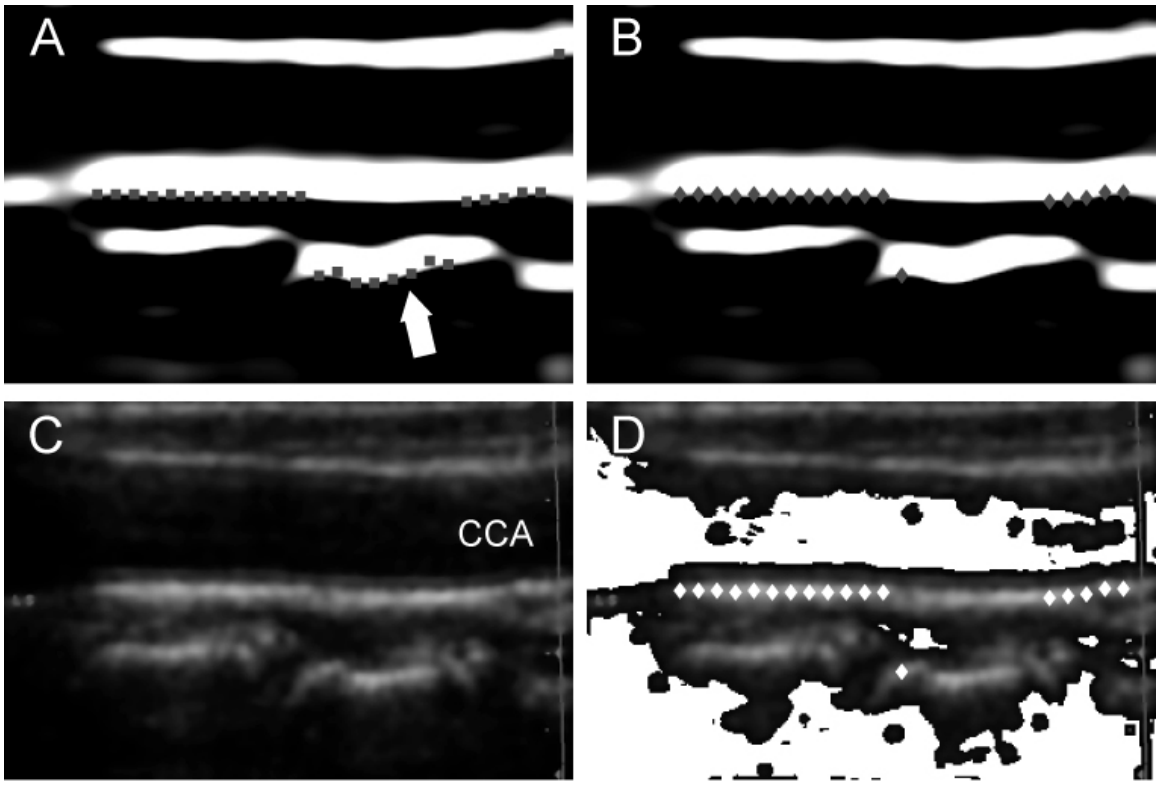

A) Downsampled and filtered image (first-order Gaussian filter) with the initial AD_F guess marked by squares. The white arrow indicates incorrect AD_F points located below the far wall that failed the lumen test and are deleted. B) The AD_F points passing the lumen check are depicted by diamonds. C) Filtered image. D) AD_F points (white diamonds) overlaid to the original image with lumen pixels in white.

Figure 5

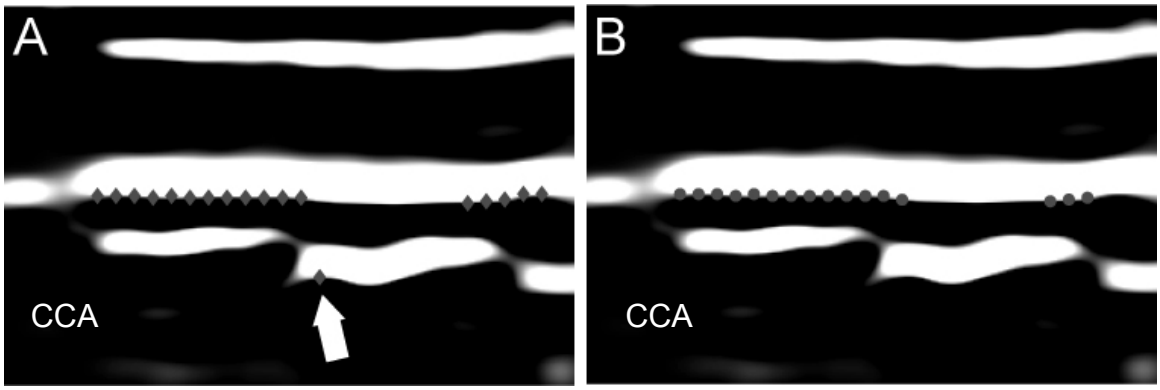

A) AD_F points (gray diamonds) that passed the lumen test. The white arrow indicates a dot located below the far wall. This point originates spikes in the AD_F profile. B) After the spike removal procedure, the AD_F points are concentrated on the far wall (gray circles).

Figure 6

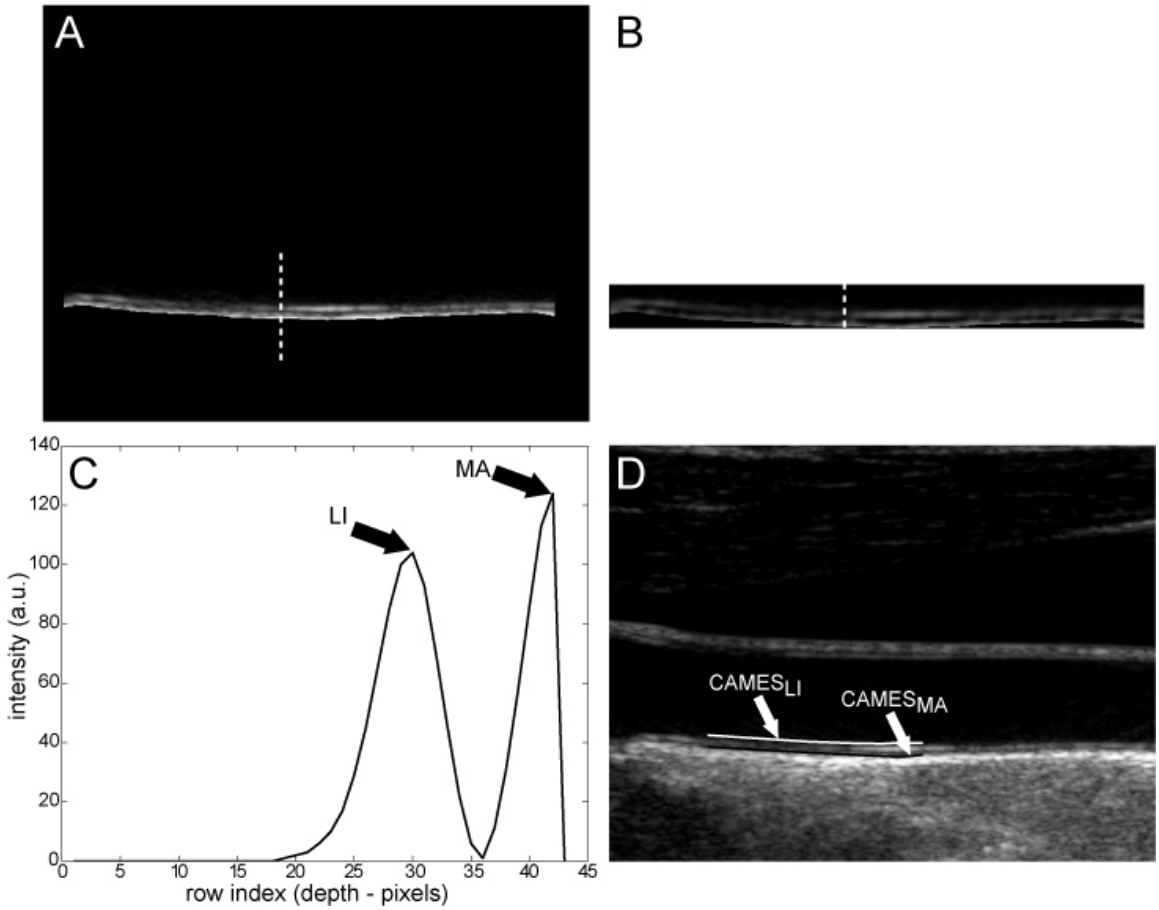

A) ROI automatically drawn around the AD_F profile (same image of fig. 4.A). B) MRAFOAM edge operator associated with the ROI of fig. 8.A. C) Intensity profile of a column of image 8.B (indicated by the vertical white dashed line). The peaks indicate the LI and MA boundaries. D) Superimposition of LI (white solid) and MA (black solid) tracings (computed by CAMES) on the cropped grayscale image.

(LI – lumen-intima interface; MA – media-adventitia interface; $CAMES_{LI}$ – LI tracing by CAMES; $CAMES_{MA}$ – MA tracing by CAMES)

Figure 7

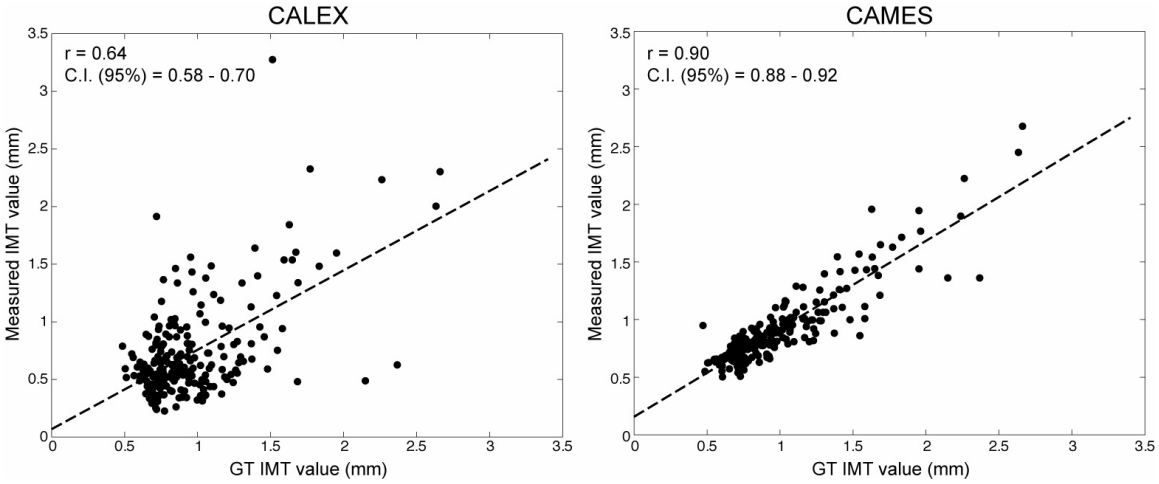

Scatter diagram for the CALEX (left panel) and CAMES (right panel) with respect to GT (depicted on the horizontal axis).

Figure 8

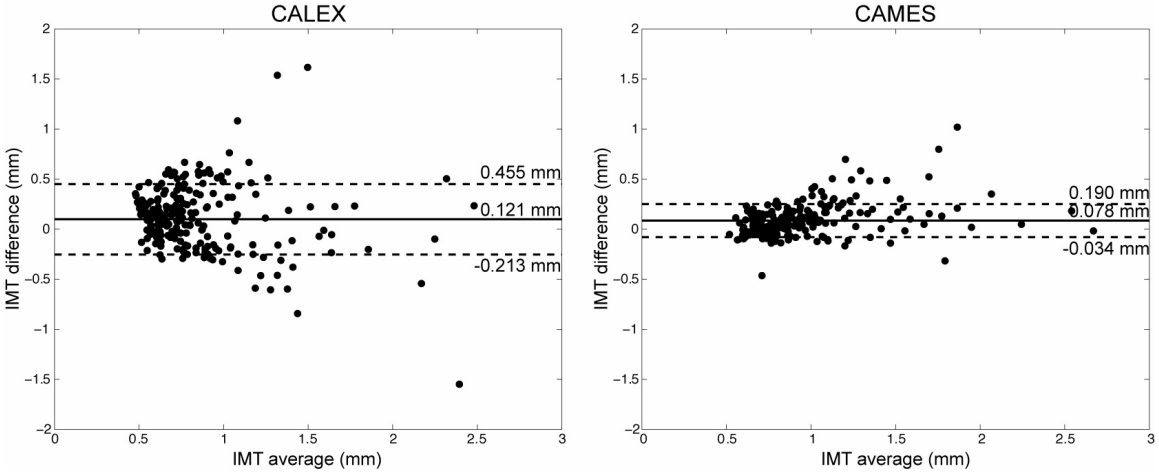

Bland-Altmann plots for CALEX (left panel) and CAMES (right panel).

Figure 9

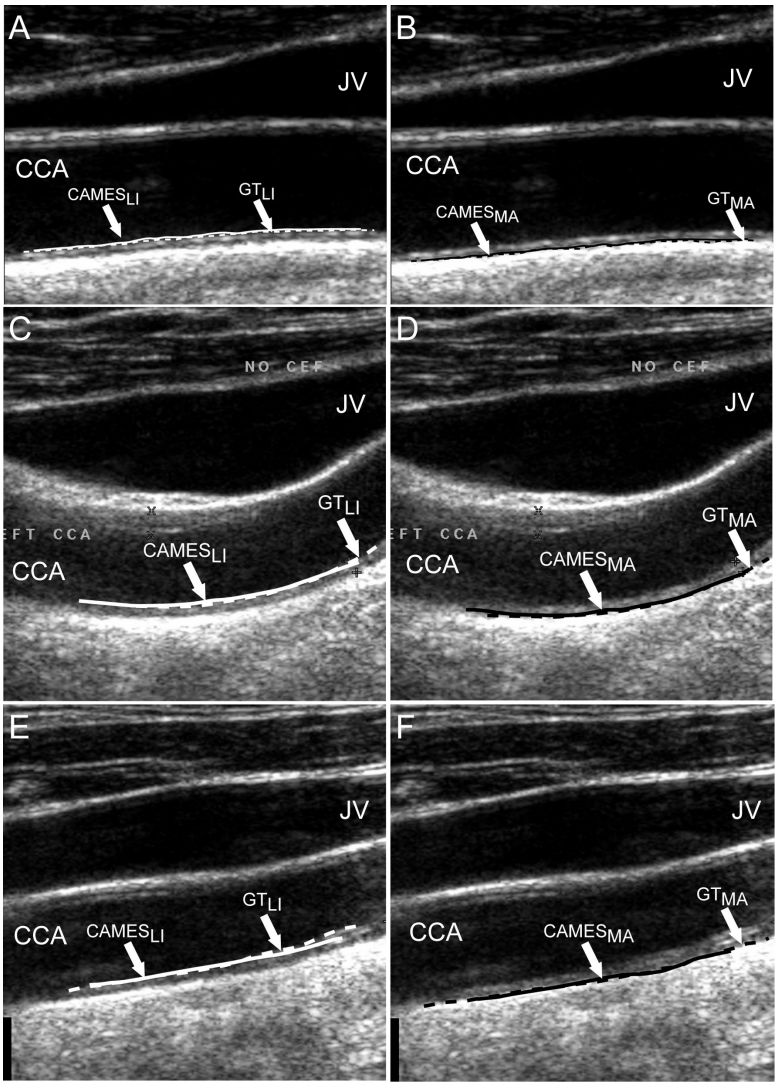

Samples of CAMES segmentation showing versatility of the technique. A-C-E) Lumen-intima segmentation and tracings. B-D-F) Media-adventitia segmentation and tracings. A) and B) are relative to a straight and horizontal carotid; C) and D) to a curved carotid, and E) and F) to a straight and inclined artery.

(CAMES$_{LI}$ – LI tracing by CAMES; CAMES$_{MA}$ – MA tracing by CAMES; GT$_{LI}$ – ground truth LI boundary; GT$_{MA}$ – ground truth MA boundary)

Biographies

Filippo Molinari, PhD, was born in Piacenza, Italy. He received the Italian Laurea degree and the Ph.D. in Electronics from the Politecnico di Torino, Torino, Italy, in 1997 and 2000, respectively. Since 2002, he is Assistant Professor on faculty of the Dept. di Electronics of the Politecnico di Torino. Since 2001, he taught courses on biomedical signal processing, biomedical image processing, and instrumentation for medical imaging. His research topics include the analysis of biosignals and the biomedical image processing applied to the computer-aided diagnosis and therapy. In the field of ultrasound imaging, Dr. Molinari developed diagnosis procedure for vascular applications and thyroid assessment. Dr. Molinari is member of the IEEE Engineering in Medicine and Biology Society (EMBS), of the Italian Group of Bioengineering (GNB), and of the American Institue for Ultrasound in Medicine (AIUM).

C. S. Pattichis (S'88–M'88–SM'99) was born in Cyprus, in January 30, 1959. He received the Diploma degree in technician engineering from the Higher Technical Institute, Nicosia, Cyprus, in 1979, the B.Sc. degree in electrical engineering from the University of New Brunswick, NB, Canada, in 1983, the M.Sc. degree in

biomedical engineering from the University of Texas, Austin, in 1984, the M.Sc. degree in neurology from the University of Newcastle Upon Tyne, U.K., in 1991, and the Ph.D. degree in electronic engineering from the University of London, London, U.K., in 1992. He is currently a Professor in the Department of Computer Science, University of Cyprus, Nicosia, Cyprus. His research interests include e-health, medical imaging, biosignal analysis, and intelligent systems. He has been involved in numerous projects in these areas funded by the European Union (EU), the National Research Foundation of Cyprus, the INTERREG, and other bodies, with a total funding managed in excess of five million Euros. He was on the Editorial Board of the Journal of Biomedical Signal Processing and Control. He is the Co-Editor of the books: M-Health: Emerging Mobile Health Systems (New York: Springer, 2006), and Information Technology in Biomedicine (IEEE, to be published in 2010). He is the coauthor of the monograph Despeckle Filtering Algorithms and Software for Ultrasound Imaging (San Rafael, CA: Morgan & Claypool, 2008). He is the author or coauthor of 52 refereed journal and 142 conference papers, and 19 chapters in books in these areas.

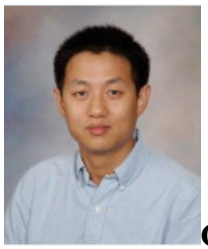

Guang Zeng received the B.S. degree from Xiangtan University, China in 1998. He received the M.S. degree in 2005 and the Ph.D. degree in 2008 from Clemson University, SC, USA, both in Electrical Engineering. He is currently working in the Aging and Dementia Imaging Research Laboratory, Mayo Clinic, Rochester, MN. His

research interests include biomedical image processing, pattern recognition and computer vision.

 **Luca Saba, MD,** received the MD degree from the University of Cagliari, Italy in 2002. Today he works in the A.O.U. of Cagliari. Dr Saba research fields are focused on Neuroradiology, Multi-Detector-Row Computed Tomography, Magnetic Resonance, Ultrasound, and Diagnostic in Vascular Sciences.

His works, as lead author, achieved more than **75** high impact factor, peer-reviewed, Journals. Dr. Saba has written 7 book chapters and he presented more than 400 papers in National and International Congress. Dr Saba is member of the Italian Society of Radiology (SIRM), European Society of Radiology (ESR), Radiological Society of North America (RSNA), American Roentgen Ray Society (ARRS) and European Society of Neuroradiology (ESNR).

 **U Rajendra Acharya, PhD, Deng,** is a Visiting faculty in Ngee Ann Polytechnic, Associate faculty in SIM University, Singapore and Adjunct faculty in Manipal Institute of Technology, Manipal, India. He received his Ph.D. from National

Institute of Technology Karnataka, Surathkal, India and DEngg from Chiba University, Japan. He has published more than **145** papers. He is in the editorial board of many journals and served as Guest Editor for many journals. His major interests are in Biomedical Signal Processing, Bio-imaging, Data mining, Visualization and Biophysics for better healthcare design, delivery and therapy.

Roberto Sanfilippo, MD,

Andrew Nicolaides, MS, FRCS, PhD (Hon) graduated from Guy's Hospital Medical School, London University, London, U.K., in 1962. He received the M.S. degree from the Royal College of Surgeons of England, London, U.K., and the F.R.C.S., and F.R.C.S.E. degrees from the Royal College of Surgeons of England, London, and the Royal College of Surgeons of Edinburgh, Midlothian, U.K., in 1967. He is currently the Professor Emeritus at Imperial College, London and an Examiner for M.S. and Ph.D. degrees for London University, London. He is also a "Special Scientist" at the University of Cyprus, Nicosia, Cyprus, and theMedical Director of theVascular Screening and Diagnostic Centre, London. His current research interests include the genetic risk factors for cardiovascular disease, identification of individuals at risk and the development of effective methods of prevention, especially stroke. He is Editor-in-Chief

of International Angiology and is on the Editorial Board of many vascular journals. He is the coauthor of more than 500 original papers and editor of 14 books.

Jasjit S. Suri, PhD, MBA, Fellow AIMBE, is an innovator, visionary, scientist, and an internationally known world leader, has spent over **25** years in the field of biomedical engineering/sciences and its management. Dr. Suri has written over **350** peer-reviewed publications. He has championed the field imaging sciences. He received his Masters from University of Illinois, Chicago, Doctorate from University of Washington, Seattle, and Executive Management from Weatherhead School of Management, CWRU, Cleveland. Dr. Suri is a committee member of several journals and companies. Dr. Suri was crowned with President's Gold medal in 1980 and the *Fellow of American Institute of Medical and Biological Engineering* (AIMBE), awarded by National Academy of Sciences, Washington DC in 2004. Dr. Suri has been the chairman of IEEE Denver section and has won over 50 awards during his career.

heart, brain, spine, thyroid, eye, vasculature, breast and prostate. He has championed the field of image segmentation and registration for image guided surgical applications. During his leadership, he has released over six different products along with the FDA approvals such as: Voyager, SenoScan and Artermis.

He received his Masters from University of Illinois, Chicago, Doctorate from University of Washington, Seattle, and Executive Management from Weatherhead School of

Management, Case Western Reserve University (CWRU), Cleveland. Dr. Suri has been board member of several international journals and conference committees. Dr. Suri was crowned with President's Gold medal in 1980 and the *Fellow of American Institute of Medical and Biological Engineering* (AIMBE), awarded by National Academy of Sciences, Washington DC in 2004. Dr. Suri has been the chairman of IEEE Denver section and has won over 50 awards during his career.